Earth Syst. Dynam. Discuss., 3, 523–560, 2012
www.earth-syst-dynam-discuss.net/3/523/2012/
doi:10.5194/esdd-3-523-2012

Earth System Dynamics Discussions

Strengthening of the hydrological cycle in future scenarios: atmospheric energy and water balance perspective

A. Alessandri[1], **P. G. Fogli**[2], **M. Vichi**[2,5], **and N. Zeng**[3,4]

[1]Agenzia Nazionale Per le Nuove Tecnologie, L'Energia e lo Sviluppo Economico Sostenibile (ENEA), Rome, Italy
[2]Centro Euro-Mediterraneo sui Cambiamenti Climatici, Bologna, Italy
[5]Istituto Nazionale di Geofisica e Vulcanologia, Bologna, Italy
[3]University of Maryland, Department of Atmospheric and Oceanic Science, College Park, MD, USA
[4]Earth System Science Interdisciplinary Center, College Park, MD, USA

Received: 27 June 2012 – Accepted: 3 July 2012 – Published: 12 July 2012

Correspondence to: A. Alessandri (andrea.alessandri@enea.it)

Published by Copernicus Publications on behalf of the European Geosciences Union.

Abstract

Future climate scenarios experiencing global warming are expected to strengthen hydrological cycle during 21st century by comparison with the last decades of 20th century. We analyze strengthening of the global-scale increase in precipitation from the perspective of changes in whole atmospheric water and energy balances. Furthermore, by combining energy and water equations for the whole atmosphere we profitably obtain constraints for the changes in surface fluxes and for the partitioning at the surface between sensible and latent components.

Above approach is applied to investigate difference in strengthening of hydrological cycle in two scenario centennial simulations performed with an Earth System model forced with specified atmospheric concentration pathways. Alongside the medium-high non-mitigation scenario SRES A1B, we considered a new aggressive-mitigation scenario (E1) with reduced fossil fuel use for energy production aimed at stabilizing global warming below 2 K. Quite unexpectedly, mitigation scenario is shown to strengthen hydrological cycle more than SRES A1B till around 2070. Our analysis shows that this is mostly a consequence of the larger increase in the negative radiative imbalance of atmosphere in E1 compared to A1B. This appears to be primarily related to the abated aerosol concentration in E1, which considerably reduces atmospheric absorption of solar radiation compared to A1B.

In contrast, last decades of 21st century (21C) show marked increase of global precipitation in A1B compared to E1, despite the fact that the two scenarios display almost same overall increase of radiative imbalance with respect to 20th century. Our results show that radiative cooling is weakly effective in A1B throughout all 21C, so that two distinct mechanisms characterize the diverse strengthening of hydrological cycle in mid and end 21C. It is only through a very large perturbation of surface fluxes that A1B achieves larger increase of global precipitation in the last decades of 21C. Our energy/water budget analysis shows that this behavior is ultimately due to a bifurcation in the Bowen ratios change between the two scenarios.

ESDD
3, 523–560, 2012

This work warns that mitigation policies, by abating aerosols, may lead to unexpected stronger intensification of hydrological cycle and associated changes that may last for decades after that global warming is effectively mitigated. On the other hand, it is here suggested that predictable components of the radiative forcing by aerosols may have the potential to effectively contribute to the decadal-scale predictability of changes in the hydrological strength.

1 Introduction

Future climate scenarios experiencing global warming are expected to somewhat strengthen global-scale hydrological cycle during 21st century (e.g. Huntington, 2006) and equilibrium precipitation sensitivity (ΔP) to change in temperature (ΔT) has been estimated to be on average $\sim$2–3 % K^{-1} (Held and Soden, 2006; Andrews et al., 2010). However, a non-equilibrium condition is what is usually found in real world so that precipitation change display marked transient variability at inter-decadal and longer time scale, which affects projections of ΔP by very large uncertainty (Johns et al., 2011; Douville et al., 2006; Feichter et al., 2004). Therefore, relationship between increase in temperature and precipitation is highly uncertain and cannot be assumed a priori (Trenberth and Shea, 2005; Trenberth et al., 2007; Lambert and Webb, 2008).

Precipitation changes are primarily constrained by the availability of precipitable water that follows from the atmospheric water balance equation (e.g. Hartman, 1994; Alessandri et al., 2007). On the other hand, including consideration of the atmospheric energy balance can further aid analysis of observed and projected precipitation changes (Andrews et al., 2009, 2010). Several works showed that precipitation also responds to the change in atmospheric radiative imbalance caused by the presence of the forcing agents such as greenhouse gases (GHGs) and aerosols (e.g. Andrews et al., 2010; Feichter et al., 2004). From the static stability point of view, heating of the atmosphere by GHGs, and the related water-vapor positive feedback, leads to more stable atmosphere, which may decrease convection and rainfall occurrence (Trenberth,

ESDD
3, 523–560, 2012

2011). That is, any perturbation to the atmospheric radiative cooling may compete or be balanced by a change in precipitation (Andrews et al., 2010). Hydrological sensitivity has been shown in previous works to be larger for the forcing by solar radiation compared to GHG effects (e.g. Andrews et al., 2009). Therefore, absorption and reflection of solar radiation by aerosols are particularly effective in reducing global-scale precipitation (Trenberth, 2011). In this respect, Feichter et al. (2004) showed that the global precipitation sensitivity to a 1-K surface air temperature change is almost 3 times higher for aerosol forcing than GHG forcing.

Recently, Johns et al. (2011) analyzed uncertainty in climate projections by comparing business-as-usual (A1B SRES; Nakicenovic and Swart, 2000) and a new aggressive mitigation scenario (E1) using the multi-model approach in the framework of ENSEMBLES project (Johns et al., 2011). They showed a significantly lower global warming and precipitation increase, for E1, in the late 21st century (21C) projection. On the other hand, quite unexpectedly they revealed robust response between the models involved in displaying larger strengthening of the hydrological cycle in E1 compared to A1B in the first part of 21st century (21C). This behavior was suggested to be related to the mitigated forcing by aerosols in E1 (Johns et al., 2011).

In this study, the strengthening of hydrological cycle is simply measured by taking the spatial-average of precipitation rate. By exploiting both water and energy conservation principles in the atmosphere, the strengthening of global-scale hydrological cycle is analyzed in one of the Earth System Models (ESMs) participating to the ENSEMBLES centennial climate projection exercise (Johns et al., 2011). The reasons for the different precipitation changes during E1 mitigation scenario compared to A1B are investigated in detail. In Sect. 2, we report the method with Sects. 2.1 and 2.2 briefly describing the ESM and the scenario pathways used, respectively. Section 2.3 defines the tool for analysis of precipitation changes based on water and energy balance equations. In Sect. 3, the results are reported analyzing the constraints to precipitation changes coming from atmospheric water (Sect. 3.1) and atmospheric energy (Sect. 3.2) conservation equations. Then, Sect. 3.3 investigates the implications for the surface partitioning

ESDD
3, 523–560, 2012

between sensible and latent heat fluxes. Finally, in Sect. 4 a discussion and a summary of conclusions will close this study.

2 Method

In this work the strength of the global-scale hydrological cycle is simply measured by the spatially-averaged rate of precipitation. The modeling data employed are the simulations performed with the CMCC Earth System Model (C-ESM; see Sect. 2.1) following the protocol of the ENSEMBLES multi-model experiment described in Johns et al. (2011) and briefly reported in Sect. 2.2.

2.1 Model

The C-ESM consists of an atmosphere-ocean-sea ice physical core coupled to land and ocean carbon cycle components. The technical description of the atmosphere-ocean coupling as well as the closure of the carbon cycle are described in Fogli et al. (2009) while the evaluation of the model in terms of global and regional ocean carbon uptake and of the related sensitivity to climate change is reported in Vichi et al. (2011). The model components are Océan PArallélisé version 8.2 (OPA8.2; Madec et al., 1998) for the ocean, ECmwf HAMburg version 5 (ECHAM5; Roeckner et al., 2003) for the atmosphere, the Louvain-la-Neuve sea ice model (LIM2; Timmerman et al., 2005), the PELAgic biogeochemistry for Global Ocean Simulations (PELAGOS) model for the ocean biogeochemistry (Vichi et al., 2007a,b) and Surface Interactive Land VegetAtion (SILVA; see description in following next paragraphs) model for the Land Surface-Vegetation component. The coupler OASIS3 (Valcke , 2006) is used to on-line exchange all relevant fields between the atmosphere and ocean components.

The SILVA model has been developed in order to suitably represent the land surface processes and the associated variability. The parameterization of the flux exchanges at the interface between land-surface and atmosphere have been implemented

ESDD
3, 523–560, 2012

and developed following the SECHIBA ("Schématisation des Echanges Hydriques á l'Interface entre la Biosphére et l'Atmosphére", Ducoudré et al., 1993) scheme approach, while the Vegetation and Carbon dynamics have been developed using the core parameterizations coming from VEGAS (VEgetation-Global-Atmosphere-Soil, Zeng et al., 2005). SILVA can integrate the vegetation-carbon dynamics fully mechanistically with the characteristics of 4 Plant Functional Types (PFTs) that have been implemented in the model in order to suitably represent vegetation diversity: broadleaf tree, needleleaf tree, cold grass and warm grass. The different photosynthetic pathways are distinguished for C3 (the first three PFTs above) and C4 (warm grass) plants. Competition between C3 and C4 grass is a function of temperature and CO_2 following Collatz et al. (1998). Each PFT may be present simultaneously in one grid element (besides bare soil). This takes into account the subgrid-scale distribution of the vegetation types and is often referred to as "mosaic approach". The surface water balance and the surface fluxes such as transpiration and direct evaporation of water stored in the canopy interception reservoir are computed separately for each fractional surface cover class. Then the total flux exchanged with the atmosphere is determined as an area-weighted average for each grid box. Phenology is simulated dynamically as the balance between growth and respiration/turnover. Competition is determined by climatic constraints and resource allocation strategy such as temperature tolerance and height dependent shading. The relative competitive advantage determines the fractional coverage of each PFT with possibility of coexistence. The vegetation dynamics is accompanied by the full terrestrial carbon cycle, starting from photosynthetic carbon assimilation in the leaves and the allocation of this carbon into three vegetation carbon pools: leaf, root and wood. After accounting for respiration, the biomass turnover from these three vegetation carbon pools cascades into a fast soil carbon pool, an intermediate and a slow soil pool at last. Temperature and moisture dependent decomposition of these carbon pools returns carbon back into atmosphere, thus closing the terrestrial carbon cycle. A natural fire module includes the effects of moisture availability, fuel loading, and PFT dependent resistance to combustion.

ESDD
3, 523–560, 2012

The SILVA representation of the land carbon cycle and of its sensitivity to climate change appears reasonably simulated, when compared to the other models participating in ENSEMBLES (Johns et al., 2011). However, the ENSEMBLES ESMs evidenced quite an high ensemble spread in the carbon fluxes among the land models, with three models projecting a decreasing but still significant land carbon sink in A1B towards 2100, while two models project carbon source. Somewhat closer agreement occurs for E1, with the ensemble mean showing a tendency towards a neutral land carbon budget. In this respect, SILVA displayed a moderate carbon source behavior on the global average and falling close to the average of the other models. For the sake of completeness, the globally integrated and accumulated land carbon uptake (GtC) simulated by SILVA during the last part of 20th century as well as through A1B and E1 scenarios are reported in Fig. 1.

2.2 Scenario pathways

The scenario simulations performed with the C-ESM are those designed in the ENSEMBLES Stream 2 (ES2) experimental framework and described in Johns et al. (2011). An historical (1860–1999) and two future scenario runs has been performed by prescribing available pathways of well mixed greenhouse gases (GHGs; Fig. 3) and aerosols (Fig. 4 reports total burden of sulfate aerosol plus SO_2) as boundary conditions. For the historical run, the annual observation-based estimates that where made available for the ENSEMBLES project (Johns et al., 2011) have been used. For the future scenario experiments, the A1B SRES (Nakicenovic and Swart, 2000) and E1 scenarios have been used. E1 was specifically developed for ENSEMBLES with the IMAGE2.4 Integrated Assessment Model (Bouwman et al., 2006; van Vuuren et al., 2007) as an aggressive mitigation scenario designed to keep anthropogenic warming below 2 K. Solar and Volcanic forcing variations were not accounted for in C-ESM simulations. For further details on scenario implementation and characteristics, refer to Johns et al. (2011).

ESDD
3, 523–560, 2012

2.3 Atmospheric energy and water balance perspective to hydrological cycle acceleration

The water vapor content in the atmosphere is a balance between the water fluxes at the lower boundary interface and the horizontal moisture flux convergence so that the equation for the atmospheric water vapor content may be written as:

$$\frac{\partial W}{\partial t} = +E_{\uparrow} - \nabla_h \cdot \boldsymbol{Q} - P \tag{1}$$

where W is the amount of water vapor contained in a unit area atmospheric column, $E_{\uparrow}$ is the evapotranspiration, P is the precipitation and $\boldsymbol{Q}$ is the vertically integrated (from the Earth's surface to the top of the atmosphere) horizontal transport of water vapor:

$$\boldsymbol{Q} = \int_{\text{surface}}^{\text{top}} \boldsymbol{V}\, q \, \mathrm{d}z \tag{2}$$

where $\boldsymbol{V}$ is the wind, q is atmospheric specific humidity, and z is the height in meters.

Following Peixoto and Oort (1992), we can simplify the general balance equation after averaging in time and in space over a region bounded by a conceptual vertical wall and conveniently rearrange the equation to recognize contributions to precipitation as follows:

$$\left\{\overline{P}\right\} = \left\{\overline{E_{\uparrow}}\right\} + \left\{-\overline{\nabla_h \cdot \boldsymbol{Q}}\right\} - \left\{\frac{\overline{\partial W}}{\partial t}\right\} \tag{3}$$

where the overbar indicates the time and the braces stand for the space average, respectively. It is important to note here that the tendency term is small, and when considering annual mean basis it can generally be neglected (e.g. Mariotti et al., 2001). A schematic diagram of the above atmospheric water balance is reported in Fig. 2a (rightmost box).

ESDD
3, 523–560, 2012

By evaluating the difference, between scenario and historical simulations, in the climatological annual-mean precipitation, as expressed in Eq. (3), we can effectively evaluate the contributions to the change of hydrological-cycle strength based on the atmospheric water conservation constraint as follows:

$$\Delta\left\{\overline{P}\right\} = \Delta\left\{\overline{E_{\uparrow}}\right\} + \Delta\left\{-\overline{\nabla_h \cdot \boldsymbol{Q}}\right\} \tag{4}$$

where Δ indicates difference between projected scenario climate and historical climatology (Fig. 2b, right box).

Further constraint to the hydrological cycle comes from the principle of conservation of total potential energy in the atmosphere (Peixoto and Oort, 1992, we neglect here changes in kinetic energy), which, by computing the vertical integral, represents the enthalpy content in the atmospheric column (H; Peixoto and Oort, 1992):

$$H = \int_{\text{surface}}^{\text{top}} (E_{\text{int}} + \phi)\,\mathrm{d}z = \int_{\text{surface}}^{\text{top}} \rho c_{\text{p}} T\,\mathrm{d}z \tag{5}$$

where E_{int} and ϕ are internal and gravitational-potential energy, respectively; ρ is the density of air, c_{p} its specific heat at constant pressure, and T temperature. Conservation principle states that changes in the atmospheric H come from the contributions from sensible heating (SH), short wave ($\boldsymbol{S}$) radiative heating, long wave ($\boldsymbol{T}$) radiative heating and latent heating (LP):

$$\frac{\partial H}{\partial t} = LP - \nabla_z \cdot \boldsymbol{S} - \nabla_z \cdot \boldsymbol{T} + \text{SH} \tag{6}$$

here $-\nabla_z$ corresponds to top of troposphere minus surface downward radiative-fluxes; SH stands for atmospheric column sensible heating and can be further decomposed into sensible flux component from the surface and atmospheric convergence component:

$$\text{SH} = \text{SH}_{\uparrow} - \nabla_h \cdot \text{SH}. \tag{7}$$

ESDD
3, 523–560, 2012

Note that following Peixoto and Oort (1992), latent heating (LP) in Eq. (6) is considered as an internal energy source, which results from release of latent heat during precipitation. On the other hand, from Eq. (3) and above discussion on water balance when considering annual-mean basis, LP comes from the surface latent-heat flux and the contribution from atmospheric convergence:

$$\left\{L\overline{P}\right\} = \left\{L\overline{E_{\uparrow}}\right\} + \left\{-L\overline{\nabla_h \cdot \boldsymbol{Q}}\right\}. \quad (8)$$

Following the same approach applied to Eq. (1), we can simplify the energy balance equation after averaging in time and in space and rearranging to recognize regional precipitation contributions as follows:

$$\left\{L\overline{P}\right\} = -\left\{-\overline{\nabla_z \cdot \boldsymbol{S}}\right\} - \left\{-\overline{\nabla_z \cdot \boldsymbol{T}}\right\} - \left\{\overline{\mathrm{SH}}\right\} + \left\{\overline{\frac{\partial H}{\partial t}}\right\}. \quad (9)$$

By analogy to the water balance equation it is generally reasonable to assume that the tendency term is small when considering climatological annual-mean basis (e.g. Peixoto and Oort, 1992; Trenberth et al., 2001). It follows that, as schematized in Fig. 2a (left boxes), the principle of conservation of atmospheric energy requires that precipitation, and the related latent heating of the atmosphere, is balanced by radiative cooling and/or sensible heat loss. Similarly to what previously applied to the water balance equation, we can take the differences between scenario projections and historical simulations to quantify the contributions to projected changes in the strength of the hydrological cycle as follows:

$$\Delta\left\{L\overline{P}\right\} = -\Delta\left\{-\overline{\nabla_z \cdot \boldsymbol{S}}\right\} - \Delta\left\{-\overline{\nabla_z \cdot \boldsymbol{T}}\right\} - \Delta\left\{\overline{\mathrm{SH}_{\uparrow}}\right\} - \Delta\left\{-\overline{\nabla_h \cdot \mathrm{SH}}\right\}. \quad (10)$$

As depicted in Fig. 2b (left box), from Eq. (10) it is required that any projected increase of precipitation must be balanced by a corresponding radiative cooling and/or a reduction in sensible heating.

ESDD
3, 523–560, 2012

Remarkably, by combining the equations for atmospheric water and energy balance (Eqs. 4 and 10) we can readily obtain important constraints on surface flux changes and in the partitioning at the surface between sensible and latent components. Specifically, equating right hand side of Eq. (4) (multiplied by L as in Eq. 8) and right hand side of Eq. (10), the ratio between sensible and latent flux variations can be conveniently represented as follows:

$$\frac{\Delta\left\{\overline{\mathrm{SH}_{\uparrow}}\right\}}{\Delta\left\{L\,\overline{E_{\uparrow}}\right\}} = -\frac{\Delta\left\{-\overline{\nabla_z \cdot (\boldsymbol{S}+\boldsymbol{T})}\right\}}{\Delta\left\{L\,\overline{E_{\uparrow}}\right\}} - \frac{\Delta\left\{-L\,\overline{\nabla_h \cdot \boldsymbol{Q}}\right\}}{\Delta\left\{L\,\overline{E_{\uparrow}}\right\}} - \frac{\Delta\left\{-\overline{\nabla_h \cdot \mathrm{SH}}\right\}}{\Delta\left\{L\,\overline{E_{\uparrow}}\right\}} - 1. \tag{11}$$

Given the amount of precipitation change, Eq. (11) states the constraint on the surface partitioning that comes from the changes in atmospheric energy and water components. On the other hand, the ratio between change of surface fluxes of Sensible heat and Latent heat (hereinafter Bowen Ratio potential; PBr) represents the potential to affect the Bowen ratio (Br) at a given time. Assuming positive changes in Latent heating from the surface, it is straightforward to show that $PBrs$ that are larger (smaller) than current value of Br will correspond to positive (negative) change in Br. It follows that PBr is the value to which Br will tend asymptotically, provided PBr is maintained constant long enough.

3 Results

The simulated climate shows a significantly lower warming response in E1 than in A1B in the late 21C projections (Fig. 5a) consistently with the GHGs concentration path (see also Fig. 3). On the other hand, the divergence in GHGs concentration pathways, with A1B increasingly exceeding E1, do not seem to dominate the temperature response in the first half of the century. In fact, the warming during the first half of the 21C in the E1 scenario often exceeds that in A1B. As documented in Johns et al. (2011), this is mostly due to the reduction of the forcing by aerosols (Fig. 4), leading to considerably

ESDD
3, 523–560, 2012

weakened aerosol cooling in E1 compared to A1B. This behavior has been shown to be a robust response of all models involved in the same experimental exercise in the framework of the ENSEMBLES project (Johns et al., 2011). Quite unexpectedly, from Fig. 5b it is shown that the global hydrological cycle strengthens more in E1 than in A1B well beyond the half of the 21C, that is after that global temperature already intersected and with a much warmer A1B. In fact, global precipitation in E1 significantly exceeds that in A1B up until almost 2070 (Fig. 5b), thus showing that the relationship between precipitation and temperature changes is only part of the story and that there are other factors acting to weaken precipitation in A1B compared to E1. This is consistent with previous works showing that precipitation also responds to the change in atmospheric radiative heating caused by the presence of the forcing agents such as GHGs and aerosols (Andrews et al., 2010). In this respect, Feichter et al. (2004) showed that the relationship between precipitation and temperature has not necessarily to be positive and that global precipitation in some cases can even decrease in conjunction with global warming. Furthermore, the larger acceleration of hydrological cycle in E1 could be consistent with previous findings that aerosol-induced forcing tends to exhibit a stronger hydrological response than GHG forcing (Feichter et al., 2004; Andrews et al., 2009).

Figure 6 shows the scenario land vs. sea averaged changes in precipitation (panel a), temperature (panel b) and bowen ratio (*Br*; panel c). Consistently with previous works (e.g. Sutton et al., 2007), it is shown that precipitation and temperature increase more over land than over ocean. However, for both E1 and A1B, the increases over land and over ocean appear in phase between each other indicating that, for each scenario, both warming and hydrology acceleration behave as global scale processes. As expected, from Fig. 6c it is shown that the *Br* tends to decrease with the strengthening of the hydrological cycle over both land and oceans (Held and Soden, 2006). However, the comparison of the time evolution between E1 and A1B shows that *Br* has transient behavior which is different from precipitation. In fact, E1 and A1B *Brs* are very similar between each other till around 2060 over both land and sea and it is only after 2060

ESDD
3, 523–560, 2012

(earlier over sea) and towards the end of 21C that the divergence of *Br* between A1B and E1 occurs.

3.1 Atmospheric water conservation constraints to hydrological cycle

In this section we analyze the difference between projected and historical precipitation climatologies by exploiting Eq. (4), which was derived in Sect. 2. As summarized in Table 1, the precipitation increase at the end of 21C, with respect to 1970–2000 climatology, amounts to 0.15–0.2 mm d^{-1} over global land (Fig. 7a) and to 0.1–0.12 mm d^{-1} over global ocean (Fig. 7b). The acceleration of hydrological cycle over global land during 21C is sustained for about two thirds by the increased evapotranspiration over continents (see Table 2, first column) and for about one third by moisture convergence from oceans (Table 2, third column) in both E1 and A1B scenarios (Fig. 7a). This has implications to continental runoff, which has to increase on average by the same amount of the change of water mass that is converged from the oceans, if the land water-storage is not changing (Hartman, 1994). Indeed simulated water storage over global land is nearly constant during 21C in both E1 and A1B (not shown), thus implying the increase in continental runoff of nearly the same amount of water that is converged through the atmosphere. Figure 8 compares the contributions to precipitation changes, with respect to 1970–2000 climate, in scenarios E1 and A1B for the middle 21C climatology (2035–2065; panel a) and for the end 21C climatology (2070–2100; panel b). In the mid 21C climatology, E1 increases precipitation more than in A1B, over both land and sea, mostly because of the larger increase in surface evaporation. A considerable contribution over land (about one third) comes from the larger increase of moisture convergence from oceans compared to A1B. On the other hand, enhanced moisture divergence over ocean in E1 partially damps the precipitation increase there. A similar relative contribution from evaporation (i.e. about two thirds) and moisture convergence (about one third) is observed for the different precipitation change at the end of 21C (Fig. 8b), but with the precipitation increase in A1B larger than for E1 in this case.

ESDD
3, 523–560, 2012

3.2 Atmospheric energy conservation constraints to hydrological cycle

This section analyzes the contributions to projected precipitation changes, compared to 1970–2000 climatology, by applying atmospheric energy conservation constraint. To this aim, it is exploited Eq. (10) (see Sect. 2), which states that change in latent heating of atmosphere due to rainfall increase (decrease) is possible provided that changes of opposite sign occur so that the atmosphere cools (warms) radiatively and/or that negative (positive) changes in sensible heating take place. The changes in the atmospheric net absorption of long-wave radiation are negative during E1 and A1B 21C scenarios over both land and ocean (Fig. 9a). According to the Stefan-Boltzmann law, this appears consistent with increased thermal emission as a response to the atmospheric warming (e.g. Trenberth, 2011). In fact, the comparison of Figs. 5a and 9a shows that the change of thermal radiation in the atmosphere follows, over both land and sea, the time progression of temperature very closely. As a result, the curves of the thermal radiation changes for E1 and A1B intersect each other around 2050 (Fig. 9a; slightly later over sea than over land) similarly to air temperature (Fig. 5a).

The atmospheric absorption of solar radiation (Fig. 9b) shows positive changes during the 21C mostly due to the effect of increased concentration of absorbing aerosols (Johns et al., 2011). However, baseline and mitigation scenarios diverge early in the 21C, with the change of solar radiation in A1B exceeding that in E1 by more than $1.5\,W\,m^{-2}$ at the end of 21C (Fig. 9b). As previously discussed, this has been shown to be primarily due to the considerably abated aerosols in E1 compared to A1B (Johns et al., 2011).

Figure 9c reports the net (solar plus thermal) change of atmospheric radiation divergence, showing that radiative cooling during the 21C always act to compensate at least in part the increase in latent heat release due to precipitation enhancements. As summarized in Table 3 (columns 1–2), radiative cooling contributes considerably more in E1 than in A1B to the precipitation increase and also comparatively more over ocean than over land. Over sea (land), radiative cooling in E1 contributes by 76.4 % (47.0 %)

ESDD
3, 523–560, 2012

and 78.3 % (52.7 %) of the precipitation increase during mid and end 21C, respectively. In comparison, A1B displays much smaller percent of radiation contribution with only 48.1 % in mid-21C and 50.9 % in end-21C considering global ocean (see Table 3). Over land the radiative cooling contribution to precipitation changes are considerably smaller, but as well displaying substantial reduction in A1B (28.4 % in mid 21C and 34.0 % in end-21C) compared to E1 (47.0 % in mid-21C and 52.7 % in end-21C). It is important to note that, by considering radiation only, the precipitation increase in E1 should always exceed A1B. However, the change of precipitation in A1B become larger after 2070 (Fig. 6a), implying that other factors come into play in the second half of the 21C. Figure 10 compares the contributions to precipitation for E1 and A1B in the middle 21C climatology (2035–2065; panel a) and in the end-21C climatology (2070–2100; panel b). In mid-21C the larger precipitation increase in E1 compared to A1B is supported, over both land and ocean, primarily by the reduced absorption of solar radiation and secondarily by increased thermal radiation loss. For the end-21C (Fig. 10b) the difference between E1 and A1B of solar and thermal radiation balance each other (see also Fig. 9) so that net radiative contribution to the difference in precipitation increase is close to zero. Here, the much larger acceleration of hydrological cycle in A1B compared to E1, over both land and ocean, is due to the marked divergence of the response in sensible heating towards end-21C (Fig. 10b). From Fig. 10b it is also shown that much of the difference in change comes from the modification of sensible heat flux from the surface, while only a small contribution is due to atmospheric sensible heat convergence (transparent bars in Fig. 10b; see also Table 3). Figure 11 schematizes the two distinct mechanisms characterizing the diverse strengthening of hydrological cycle in mid and end 21C. In mid-21C it is the larger radiative cooling that determines higher precipitation. On the other hand, what dominates the stronger A1B hydrology in end-21C is the major reduction of surface sensible heat.

ESDD
3, 523–560, 2012

3.3 Implications for the surface sensible and latent flux

The increase of precipitation is unavoidably coupled to the surface processes. As mentioned in Sect. 3.1, it has consequences to continental runoff, which is expected to increase by the same amount of the water mass that is converged from the ocean through the atmosphere (except for changes in water mass storage over land). In this section we analyze the implications for the surface flux partitioning between sensible and latent heat. Through Eq. (11), the *PBr* is defined as the ratio between change of surface fluxes of sensible and latent heat, and it is expressed as a function of the different contributing terms coming from the atmospheric water and energy equations. The results are reported in Fig. 12 for both the mid-21C (panel a) and the end-21C (panel b).

As previously mentioned, *Br* tends to decrease all along 21C for E1 and A1B scenarios (Fig. 6c), and this is according with the negative *PBr* values in Fig. 12. The −1.0 values of the first histogram-group on the left of Fig. 12 indicate *PBrs* if surface sensible-heating reduction would be the only factor compensating for the increased atmospheric energy coming from surface latent-heat flux. For both E1 and A1B, there are other terms acting to compensate the input of latent heat from the surface. As shown in Fig. 12, absolute value of *PBr* over land (ocean) is reduced (increased) by enhanced (decreased) divergence of sensible heat through the atmosphere. On the other hand, increased (reduced) atmospheric convergence of latent heat reduces (increases) absolute value of land (ocean) *PBr*. However, in both mid-21C (Fig. 12a) and end-21C (Fig. 12b) and over both land and ocean, changes of sensible and latent heat convergence terms balance each other very closely so that they have no appreciable overall effect on *PBr*. Therefore, according to Eq. (11), the increased radiative cooling and the reduced sensible heat flux (*PBr*) are the factors that dominate and that compete in counterbalancing the increased evapotranspiration. For both land and ocean, the most important term for E1 acting to compensate the increased latent heat from surface is the larger radiative cooling (Fig. 12). On the other hand, it is the *PBr* term

ESDD
3, 523–560, 2012

(i.e. decrease of surface sensible heat) that dominates in A1B. The difference between E1 and A1B is highest in the end-21C and in particular over land (Fig. 12b), where atmospheric net radiation (R_{net}) change is very effective in E1 ($-\frac{\Delta-(\nabla_z \cdot R_{\mathrm{net}})}{\Delta \mathrm{LE}_{\uparrow}} = 0.9$ in E1 vs. 0.5 in A1B). It is important to note here that, by only considering atmospheric water/energy balances, we are able to constraint and interpret the different behavior of *PBr* in E1 and A1B during the second half of 21C. Specifically, from above analysis it is implied that bifurcation of *Br* (Fig. 6c) is strictly required in order to get the transition to the larger acceleration of hydrological cycle in A1B compared to E1. Interestingly, for both E1 and A1B, *PBr* over ocean is always larger in absolute value compared to land. This suggests that the limited availability of water for land may play a role here by favoring relatively more sensible heat in the competition for flux partitioning at the surface (Sutton et al., 2007).

4 Discussion and conclusions

Compared to baseline (SRES A1B), mitigation scenario (E1) effectively reduces global warming and hydrology acceleration in the C-ESM by the end of 21st Century (21C). On the other hand E1 warms relative to A1B in the early 21C (until about 2050) and precipitation increases more in E1 than in A1B till nearly 2070, thus displaying the weakness of the relationship between global precipitation and temperature.

Our analysis shows that, in both E1 and A1B scenarios, the acceleration of hydrological cycle over global land during 21C is sustained for about two thirds (E1: 67.4 % in mid-21C [2035–2065] and 63.8 % in end-21C [2070–2100]; A1B: 65.8 % in mid-21C and 65.5 % in end-21C) by the increased evapotranspiration over continents and for about one third (E1: 32.6 % in mid-21C and 36.2 % in end-21C; A1B: 34.2 % in mid-21C and 34.5 % in end-21C) by moisture convergence from oceans. On the other hand, moisture divergence reduces the precipitation increase over ocean for both E1 (−19.8 % in mid-21C and −21.6 % in end-21C) and A1B (−23.9 % in mid-21C and −25.8 % in end-21C). We show that, in the mid 21C climatology, E1 increases

ESDD
3, 523–560, 2012

precipitation more than A1B, over both land and sea, mostly because of the larger increase in surface evaporation. A considerable contribution over land (about one third) also comes from the larger increase of moisture convergence from oceans compared to A1B. Interestingly, similar contributions to the difference in precipitation change (about two thirds from evaporation and one third from moisture convergence) is observed for both mid and end 21C climatologies, despite of the fact that it is A1B that increases more global precipitation in the end-21C.

Through the application of the principle of conservation of energy in the atmosphere, we show that the larger strengthening of hydrological cycle in E1 than A1B till around 2070 is mostly due to higher levels of radiative cooling (primarily reduced absorption of solar radiation) of the atmosphere in E1. Consistently with mechanism described in previous works (Feichter et al., 2004; Andrews et al., 2009), this appears to follow at least in part from abated aerosol concentration compared to A1B. For the end-21C climatology, the difference of the projected change in solar and thermal radiation, between E1 and A1B, balance each other so that net radiative contribution to differential change in precipitation is close to zero. On the other hand, it is the marked difference in surface-flux partitioning in the end-21C, with considerably larger reduction in surface sensible heat-flux towards atmosphere for A1B, that feeds the much larger acceleration of hydrological cycle compared to E1 over both land and ocean.

Hydrology acceleration leads to increased energy availability in the atmosphere due to latent-heat release during precipitation. The corresponding increase in surface latent-heat flux would require a −1.0 value of the Bowen Ratio Potential (PBr; defined as the ratio between projected changes in surface sensible heat vs latent heat) if the only factor compensating for the latent-heat released in the atmosphere is the reduction of sensible heating from the surface. However, we show that other factors may contribute to compensate the atmospheric energy enhancement due to hydrology acceleration, thus leading to less negative PBr values. These factors are the increase in atmospheric divergence of sensible heat, the increase of atmospheric convergence of latent heat and the enhancement of atmospheric radiative cooling. In both mid-21C

ESDD
3, 523–560, 2012

and end-21C and over both land and ocean, it is found that the changes of sensible and latent heat convergence terms balance very closely between each other so that they have no appreciable overall effect on PBr. Apart from this common characteristic, our results show that baseline and mitigation scenarios behave very differently and two distinct mechanisms characterize the diverse strengthening of hydrological cycle in mid and end 21C. What dominates in E1 throughout middle to end 21C is the increase of atmospheric radiative cooling which always displays an absolute value of the ratio with latent-heat change larger than 0.5. Differently, in the baseline scenario radiative cooling is weakly effective, at least in part because of the unabated atmospheric aerosols there. This determines a drastic perturbation of surface flux partitioning in A1B with large negative PBr values during the second half of 21C. It follows the marked bifurcation of the Bowen Ratio between E1 and A1B, which ultimately induces the corresponding larger strengthening of the hydrological cycle in A1B during the last decades of projected 21C.

The methodological approach proposed in this work has proven useful in improving our understanding of the contributions to projected strengthening of hydrological cycle and of the different behavior of considered baseline and mitigation scenarios. Importantly, we warn that mitigation policies, by abating aerosols, may lead to unexpected larger increase of global precipitation that may last for decades after that global warming is effectively mitigated. A recent paper by van Oldenborgh et al. (2012) suggests that decadal climate predictions may have skill due to predictable components in the boundary conditions such as GHGs and atmospheric aerosols. Our results display that radiative forcing by aerosols may be particularly effective in perturbing global hydrological strength at decadal time-scale. In particular, it is shown that the effect of aerosols may even overcome, at this relatively short time-scale, the underlying precipitation coupling with global warming, which on the other hand is mostly related to projected increase of GHGs. We suggest that predictable components of the radiative forcing by aerosols may have the potential to effectively contribute to the decadal-scale predictability of changes in the hydrological strength.

ESDD
3, 523–560, 2012

Acknowledgements. This work was supported by the ENSEMBLES project, funded by the European Commission's 6th Framework Program through contract GOCE-CT-2003-505539. M. Vichi and P. G. Fogli acknowledge the support of the Italian Ministry of Education, University and Research and the Ministry for Environment, Land and Sea through the project GEMINA.

References

Alessandri, A., Gualdi, S., Polcher, J., and Navarra, A.: Effects of Land Surface-Vegetation on the Boreal Summer Surface Climate of a GCM, J. Climate, 20, 255–277, 2007. 525

Andrews, T., Forster, P. M., and Gregory, J. M.: A surface energy perspective on climate change, J. Climate, 22, 2557–2570, doi:10.1175/2008JCLI2759.1, 2009. 525, 526, 534, 540

Andrews, T., Forster, P. M., Boucher, O., and Bellouin, N.: Precipitation, radiative forcing and global temperature change, Geophys. Res. Lett., 37, L14701, doi:10.1029/2010GL043991, 2010. 525, 526, 534

Bonan, G.: Ecological Climatology: Concepts and Applications, Cambridge University Press, Cambridge, 550 pp., 2008.

Bouwman, L., Kram, T., and Klein-Goldewijk, K.: Integrated Modelling of Global Environmental Change, An Overview of IMAGE 2.4, Netherlands Environmental Assessment Agency, Bilthoven, 2006. 529

Collatz, G. J., Berry, J. A., and Clark, J. S.: Effects of climate and atmospheric CO_2 partial pressure on the global distribution of C-4 grasses: present, past, and future, Oecologia, 114, 441–454, 1998. 528

Douville, H., Salas-Melia, D., and Tyteca, S.: On the tropical origin of uncertainties in the global land precipitation response to global warming, Clim Dynam., 26, 367–385, 2006. 525

Ducoudré, N., Laval, K., and Perrier, A.: SECHIBA, a New Set of Parameterizations of the Hydrologic Exchanges of the Land-Atmosphere Interface within the LMD Atmospheric General Circulation Model, J. Climate, 6, 248–273, 1993. 528

Feichter, J., Roeckner, E., Lohmann, U., and Liepert, B.: Nonlinear aspects of the climate response to greenhouse gas and aerosol forcing, J. Climate, 17, 2384–2398, 2004. 525, 526, 534, 540

ESDD

3, 523–560, 2012

Fogli, P. G., Manzini, E., Vichi, M., Alessandri, A., Gualdi, S., Scoccimarro, E., Masina, S., and Navarra, A.: INGV-CMCC Carbon: A Carbon Cycle Earth System Model, CMCC Tech. Rep. RP0061, http://www.cmcc.it/publications-meetings/publications/research-papers/rp0061-ingv-cmcc-carbon-icc-a-carbon-cycle-earth-system-model (last access: June 2012), 2009. 527

Hartman, D. L.: Global Physical Climatology, in: International Geophysics Series, edited by: Dmowska, R. and Holton, J. R., Academic Press, 56, 411 pp., 1994. 525, 535

Held, I. M. and Soden, B. J.: Robust responses of the hydrological cycle to global warming, J Climate, 19, 5686–5699, 2006. 525, 534

Huntington, T. G.: Evidence for intensification of the global water cycle: review and synthesis, J. Hydrol., 319, 83–95, 2006. 525

Johns, T. C., Royer, J.-F., Hoschei, I., Huebener, H., Roeckner, E., Manzini, E., May, W., Dufresne, J.-L., Ottera, O. H., van Vuuren, D. P., Salas y Melia, D., Giorgetta, M. A., and Hewitt, C. D.: Climate change under aggressive mitigation: the ENSEMBLES multi-model experiment, Clim. Dynam., 37, 1975–2003, doi:10.1007/s00382-011-1005-5, 2011. 525, 526, 527, 529, 533, 534, 536

Lambert, F. H. and Webb, M. J.: Dependency of global mean precipitation on surface temperature, Geophys. Res. Lett., 35, L16706, doi:10.1029/2008GL034838, 2008. 525

Madec, G., Delecluse, P., Imbard, M., and Levy, C.: OPA version 8.1 Ocean General Circulation Model reference manual, Technical report, LODYC/IPSL Note 11, Institut Pierre-Simon Laplace, Paris, France, 1998. 527

Mariotti, A., Struglia, M. V., Zeng, N., and Lau, K.-M.: The Hydrological Cycle in the Mediterranean Region and Implications for the Water Budget of the Mediterranean Sea, J. Climate, 15, 1674–1690, 2001. 530

Nakicenovic, N. and Swart, R. (Eds.): Special Report on Emissions Scenarios, A Special Report of Working Group III of the Intergovernmental Panel on Climate Change, ISBN 0521804930, Cambridge University Press, Cambridge, UK, 728 pp., 2000. 526, 529

Peixoto, J.P., and A.H. Oort, 1992: *Physics of climate*; American Institute of Physics (AIP), New York. 530, 531, 532

Roeckner, E., Bauml, G., Bonaventura, L., Brokopf, R., Esch, M., Giorgetta, M., Hagemann, S., Kirchner, I., Kornblueh, L., Manzini, E., Rhodin, A., Schlese, U., Schulzweida, U., and Tompkins, A.: The atmospheric general circulation model ECHAM5, Part I: Model description, Rep. No. 349, Max-Planck-Institut für Meteorologie, Hamburg, Germany, 127 pp., 2003. 527

ESDD
3, 523–560, 2012

Sutton, R. T., Dong, B., and Gregory, J. M.: Land/sea warming ratio in response to climate change: IPCC AR4 model results and comparison with observations, Geophys. Res. Lett., 34, L02701, doi:10.1029/2006GL028164, 2007. 534, 539

Timmermann, R., Goosse, H., Madec, G., Fichefet, T., Etheb, C., and Duliere, V.: On the representation of high latitude processes in the ORCA-LIM global coupled sea ice ocean model, Ocean Modell., 8, 175–201, 2005. 527

Trenberth, K. E.: Changes in precipitation with climate change, Clim. Res., 47, 123–138, doi:10.3354/cr00953, 2011. 525, 526, 536

Trenberth, K. E. and Shea, D.J.: Relationship between precipitation and surface temperature, Geophys. Res. Lett., 32, L14703, doi:10.1029/2005GL022760, 2005. 525

Trenberth, K. E., Caron, J. M., and Stepaniak, D. P.: The atmospheric energy budget and implications for surface fluxes and ocean heat transports, Clim. Dynam., 17, 259–276, 2001. 532

Trenberth, K. E., Jones, P. D., Ambenje, P., Bojariu, R., Easterling, D., Klein Tank, A., Parker, D., Rahimzadeh, F., Renwick, J. A., Rusticucci, M., Soden, B., and Zhai, P.: Observations: Surface and Atmospheric Climate Change, in: Climate Change 2007: The Physical Science Basis. Contribution of Working Group I to the Fourth Assessment Report of the Intergovernmental Panel on Climate Change, edited by: Solomon, S., Qin, D., Manning, M., Chen, Z., Marquis, M., Averyt, K. B., Tignor, M., and Miller, H. L., Cambridge University Press, Cambridge, UK and New York, NY, USA, 2007. 525

Valcke, S.: OASIS3 User Guide (prism_2-5), PRISM Report No. 2, 6th Edn., CERFACS, Toulouse, France, 64 pp., 2006. 527

van Oldenborgh, G. J., Doblas-Reyes, F.-J., Wouters, B., and Hazeleger, W.: Decadal prediction skill in a multi-model ensemble, Clim. Dynam., 38, 1263–1280, doi:10.1007/s00382-012-1313-4, 2012. 541

van Vuuren, D., den Elzen, M., Lucas, P., Eickhout, B., Strengers, B., van Ruijven, B., Wonink, S., and van Houdt, R.: Stabilizing greenhouse gas concentrations at low levels: an assessment of reduction strategies and costs, Climatic Change, 81, 119–159, doi:10.1007/s10584-006-9172-9, 2007. 529

Vichi, M., Pinardi, N., and Masina, S.: A generalized model of pelagic biogeochemistry for the global ocean ecosystem, Part I: theory, J. Mar. Syst., 64, 89–109, 2007a. 527

ESDD
3, 523–560, 2012

Vichi, M., Masina, S., and Navarra, A.: A generalized model of pelagic biogeochemistry for the global ocean ecosystem, Part II: numerical simulations, J. Mar. Syst., 801, 110–134, 2007b. 527

Vichi, M., Manzini, E., Fogli, P. G., Alessandri, A., Patara, L., Scoccimarro, E., Masina, S., and Navarra, A.: Global and regional ocean carbon uptake and climate change: Sensitivity to an aggressive mitigation scenario, Clim. Dynam., 37, 1929–1947, doi:10.1007/s00382-011-1079-0, 2011. 527

Zeng, N., Mariotti, A., and Wetzel, P.: Terrestrial Mechanisms of Interannual CO_2 Variability, Global Biogeochem. Cy., 19, 2539–2558, 2004. 528

ESDD

3, 523–560, 2012

Table 1. Change of (1st row) precipitation, (2nd row) temperature, (3rd row) Bowen Ratio (Br) and (4th row) ratio of rainfall vs temperature change for 2071–2100 and with respect to 1970–2000 climatology. Global land (ocean) averages in left (right) columns.

	Global land		Global ocean	
	E1	A1B	E1	A1B
Δ Rain	0.15	0.20	0.10	0.12
Δ Temp	2.3	3.8	1.5	2.5
ΔBr	−0.05	−0.11	−0.02	−0.03
$\frac{\Delta \text{Rain}}{\Delta \text{Temp}}$	0.065 (3.73 $\frac{\%}{K}$)	0.053 (3.00 $\frac{\%}{K}$)	0.066 (2.15 $\frac{\%}{K}$)	0.048 (1.55 $\frac{\%}{K}$)

ESDD
3, 523–560, 2012

Table 2. E1 vs. A1B contributions to rainfall change coming from surface evaporation (Evap) and atmospheric moisture convergence (Moist Conv) for (upper rows) 2035–2065 (mid-21C) and for (lower rows) 2071–2100 (end-21C) with respect to 1970–2000 climatology. Global land (ocean) averages in left (right) columns for each contributing factor.

Contributions (%) to Rainfall Change from atmospheric water conservation					
		Evap		Moist Conv	
Climatology	Scenario	Land	Sea	Land	Sea
Mid-21C (2035–2065)	E1	67.4	119.8	32.6	−19.8
	A1B	65.8	123.9	34.2	−23.9
End-21C (2070–2099)	E1	63.8	121.6	36.2	−21.6
	A1B	65.5	125.8	34.5	−25.8

ESDD
3, 523–560, 2012

Table 3. Same as Table 2 but for contributions to rainfall coming from (left) atmospheric radiation, (middle) surface sensible heat flux and (right) atmospheric sensible-heat convergence.

Contributions (%) to Rainfall Change from atmospheric energy conservation							
		Radiation		Sensible heat Surf.		Sensible heat Conv	
Climatology	scenario	Land	Sea	Land	Sea	Land	Sea
Mid-21C	E1	47.0	76.4	21.4	57.6	31.5	−34.0
(2035–2065)	A1B	28.4	48.1	36.2	92.1	35.3	−38.9
End-21C	E1	52.7	78.3	17.6	52.5	29.6	−30.8
(2070–2099)	A1B	34.0	50.9	33.7	83.2	32.2	−39.9

ESDD
3, 523–560, 2012

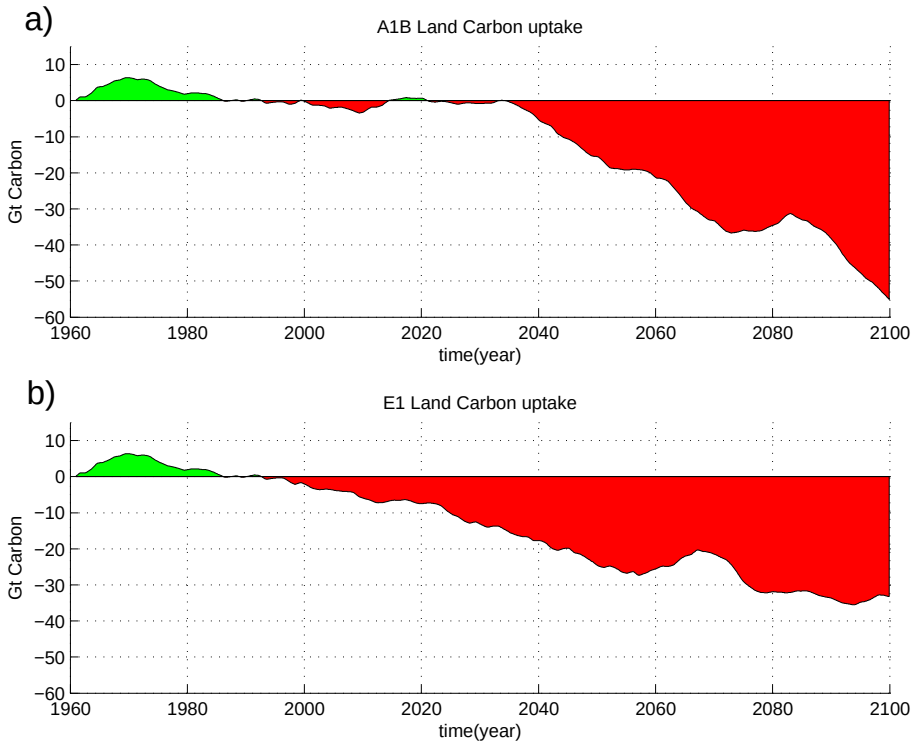

Fig. 1. Globally integrated and accumulated Land Carbon uptake (GtC) during the last part of 20th century and through the **(a)** A1B and **(b)** E1 21st century scenario, respectively. Green (red) stand for positive (negative) uptakes with respect to 1960.

ESDD
3, 523–560, 2012

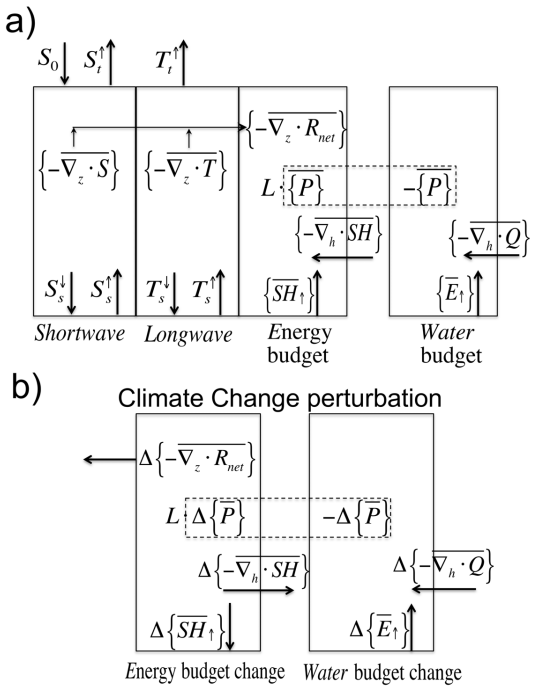

Fig. 2. Schematic diagram showing notation for **(a)** the atmospheric energy and water budgets and **(b)** perturbation of atmospheric energy and water budgets following climate-change related precipitation increase. For both energy and water, the terms of the budgets (and budget changes) are displayed so that they sum to zero following Eqs. (3), (4), (9) and (10). Rightmost boxes show atmospheric water budget while left boxes display the corresponding energy budgets. In **(a)**, proceeding from left to right, the tree boxes on the left show atmospheric shortwave, longwave and total energy budgets, respectively. S and T denote shortwave and longwave radiative fluxes, respectively, with arrows indicating upward or downward direction. Subscripts s, t and o stand for surface, top of the atmosphere and solar constant, respectively. R_{net} is the net radiative flux as the sum of longwave and shortwave components.

ESDD
3, 523–560, 2012

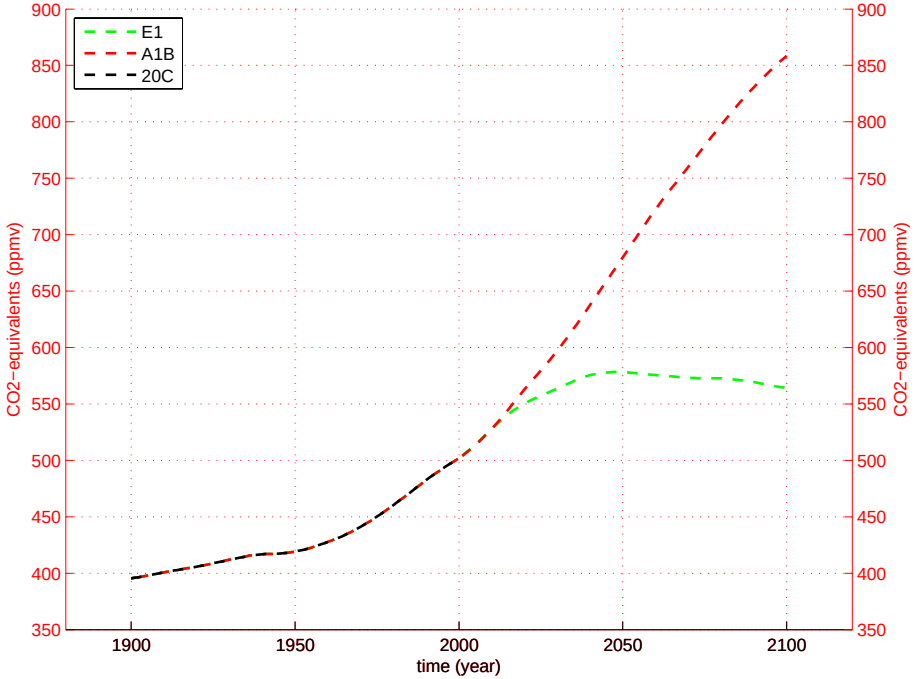

Fig. 3. Evolution of the prescribed Greenhouse Gases expressed as concentration of CO_2-equivalents (ppmv) for the historical observed period 1900–2000 (20C; black curve) and for the different scenarios. A1B (red) is the IPCC SRES marker scenario. E1 (green) is the mitigation scenario produced by the IMAGE integrated assessment model.

ESDD
3, 523–560, 2012

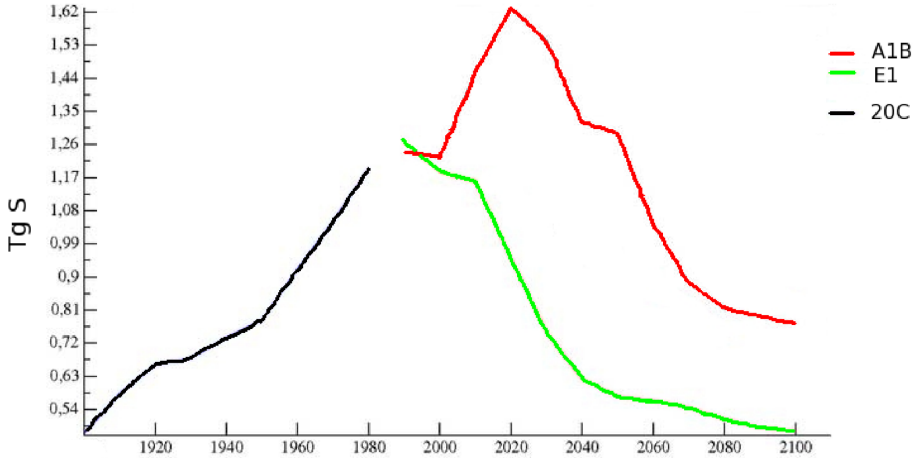

Fig. 4. Evolution of prescribed total sulfate burden (TgS of total sulfate aerosol plus SO_2) for the historical observed period 1900–2000 (20C; black curve) and for the different scenarios. A1B (red) is the IPCC SRES marker scenario. E1 (green) is the mitigation scenario produced by the IMAGE integrated assessment model.

ESDD
3, 523–560, 2012

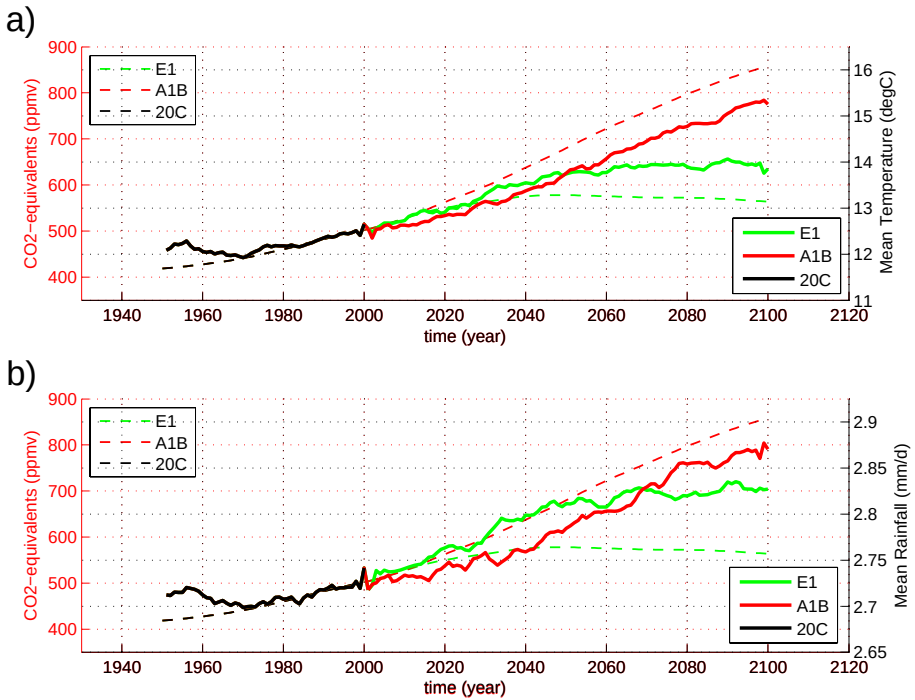

Fig. 5. Time evolution of 5-yr running mean globally-averaged **(a)** near surface temperature and **(b)** precipitation (right axis solid lines) vs. GHGs concentration (left axis dashed lines) for the historical observed period 1950–2000 (20C; black), for A1B (red) and E1 (green).

ESDD
3, 523–560, 2012

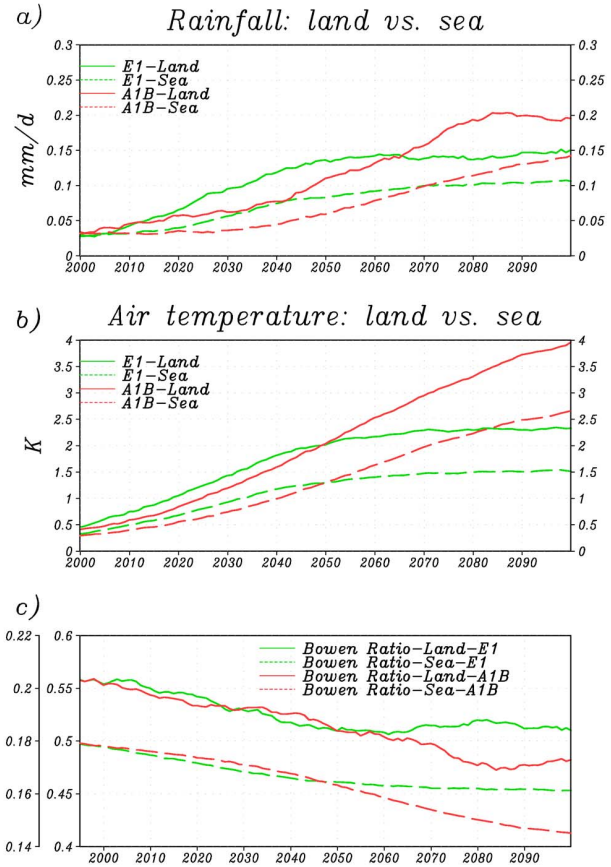

Fig. 6. Time evolution of 15-yr running means for land averaged (solid lines) and sea averaged (dashed lines) change of **(a)** precipitation (mm d^{-1}) and **(b)** near surface temperature (K) relative to 1970–2000 climatology. **(c)** is bowen ratio evolution with inner axis for land and outer axis for ocean. A1B in red and E1 green.

ESDD
3, 523–560, 2012

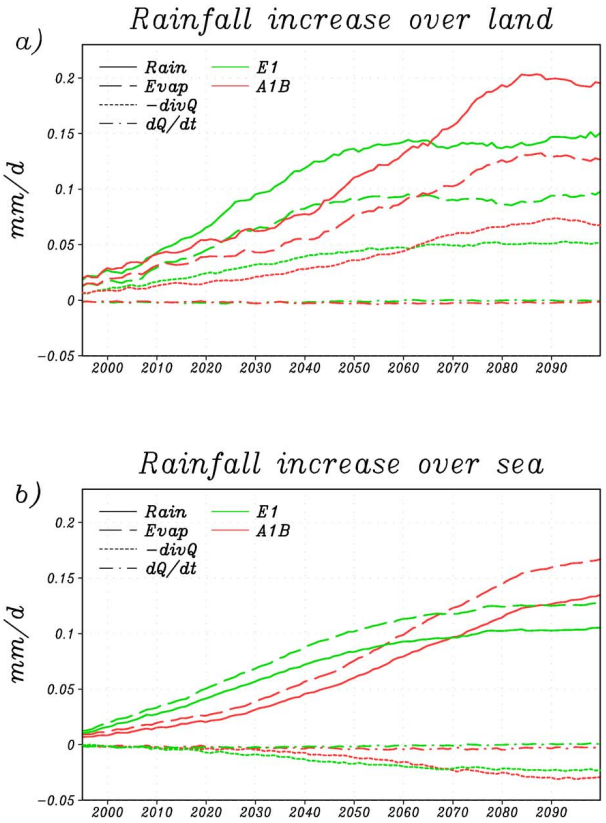

Fig. 7. Time evolution of 15-yr running means for **(a)** land averaged and **(b)** sea averaged contribution to rainfall change (solid lines) coming from local evapotranspiration (dashed lines), moisture convergence (dotted) and from change in atmospheric total water content (dash-dot lines). A1B in red and E1 green.

ESDD
3, 523–560, 2012

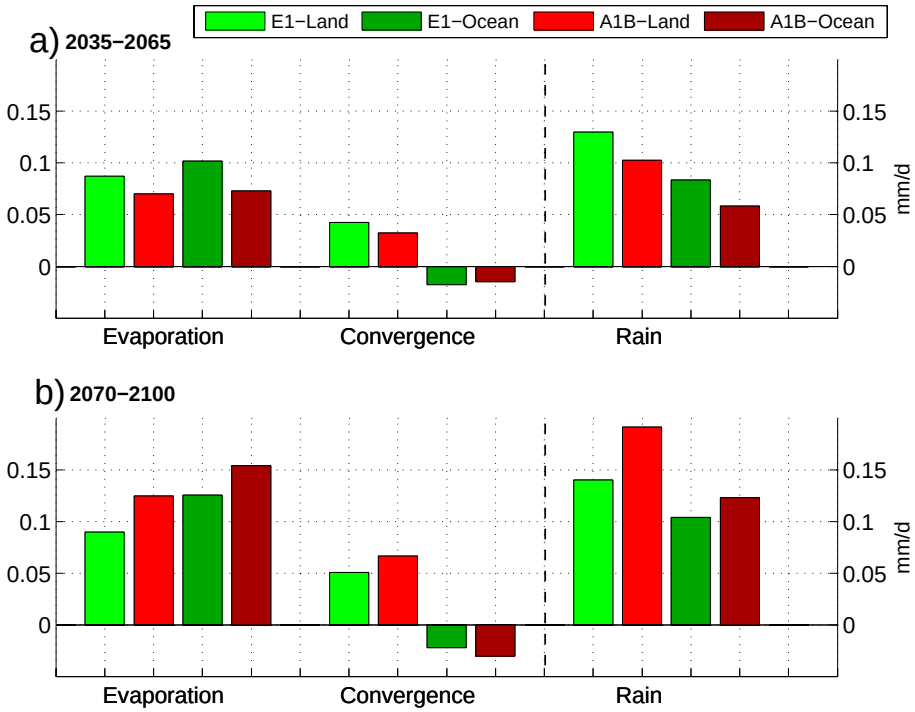

Fig. 8. Land averaged (light colors) and sea averaged (dark colors) contributions to rainfall change coming from local evapotranspiration and moisture convergence for **(a)** 2035–2065 and **(b)** 2070–2100 averages and compared to reference 1970–2000 climatology. A1B in red and E1 green.

ESDD
3, 523–560, 2012

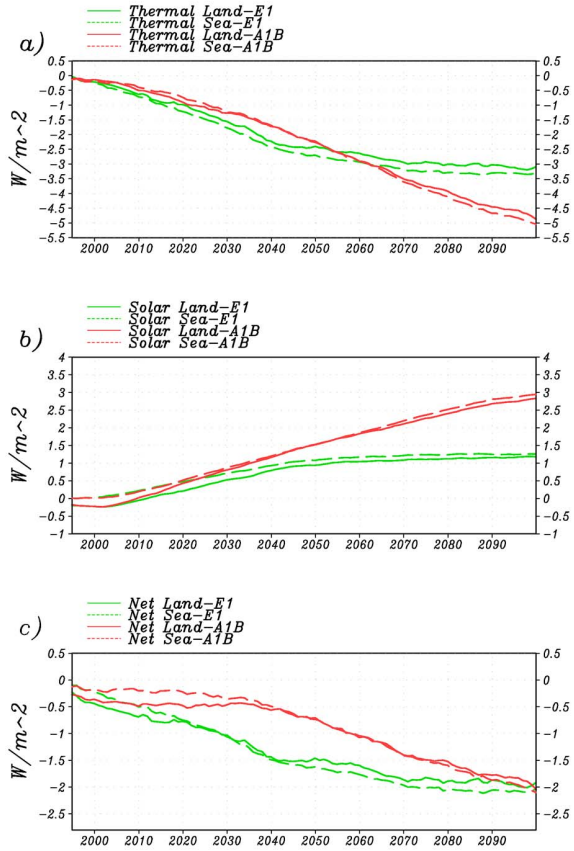

Fig. 9. 15-yr running means of the change in atmospheric vertical divergence for of **(a)** thermal radiation **(b)** solar radiation and **(c)** net (solar + thermal) radiation by comparison with reference 1970–2000 climatology. Land averages (solid lines) and sea averages (dashed lines) are reported for both (red) A1B and (green) E1 scenarios.

ESDD
3, 523–560, 2012

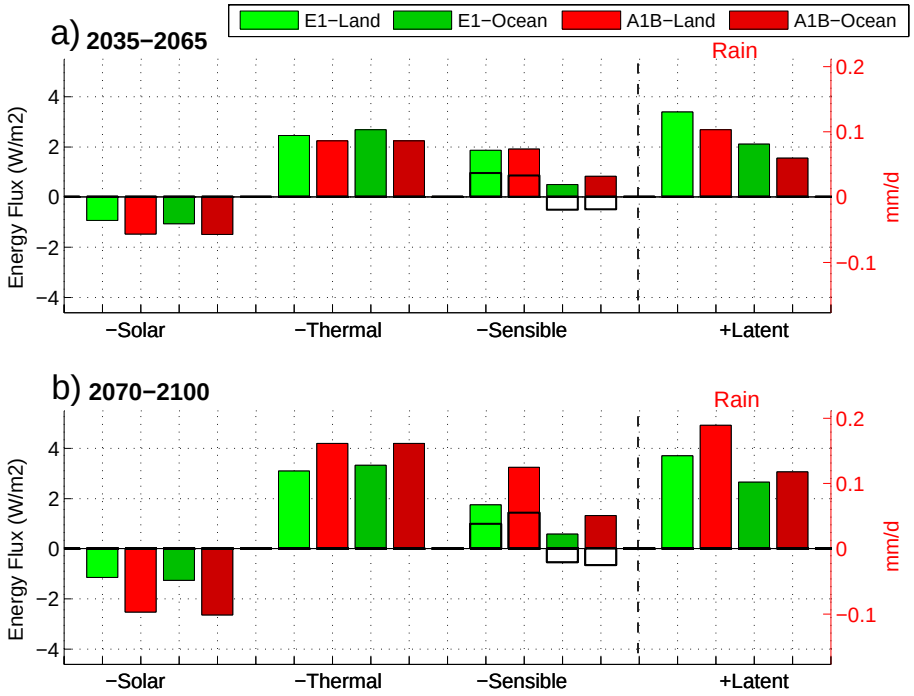

Fig. 10. Land averaged (light colors) and sea averaged (dark colors) contributions to rainfall change coming from variation in atmospheric absorption of solar radiation, thermal radiation and sensible heating for **(a)** 2035–2065 and **(b)** 2070–2100 averages and compared to reference 1970–2000 climatology. A1B in red and E1 green. For the sensible heating, contribution from atmospheric convergence is reported with transparent bars.

ESDD
3, 523–560, 2012

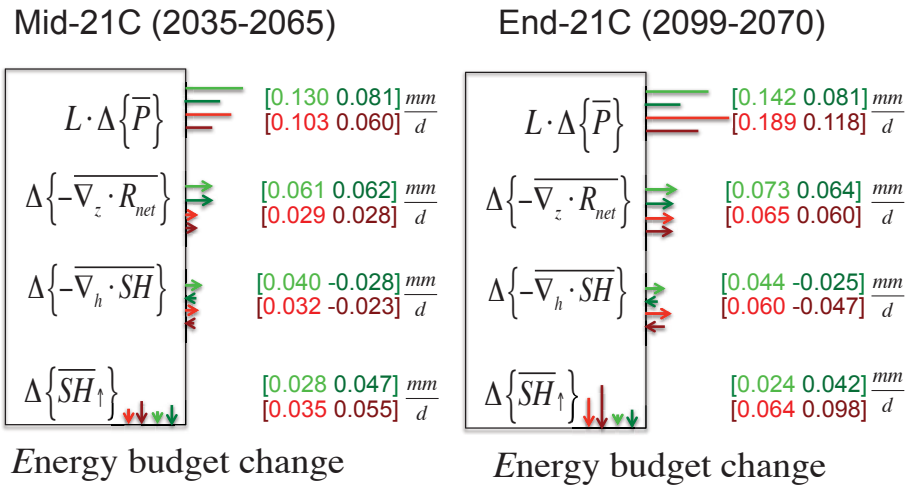

Fig. 11. Schematization of the two distinct mechanisms characterizing the diverse strengthening of hydrological cycle in mid (left box) and end (right box) 21C. The atmospheric energy balance perturbation is reporter as in Fig. 2b (left box) and colored numbers/arrows indicate precipitation change and the corresponding contributions coming from each term of energy balance. Land averages (light colors) and sea averages (dark colors) are red for A1B and green for E1.

ESDD
3, 523–560, 2012

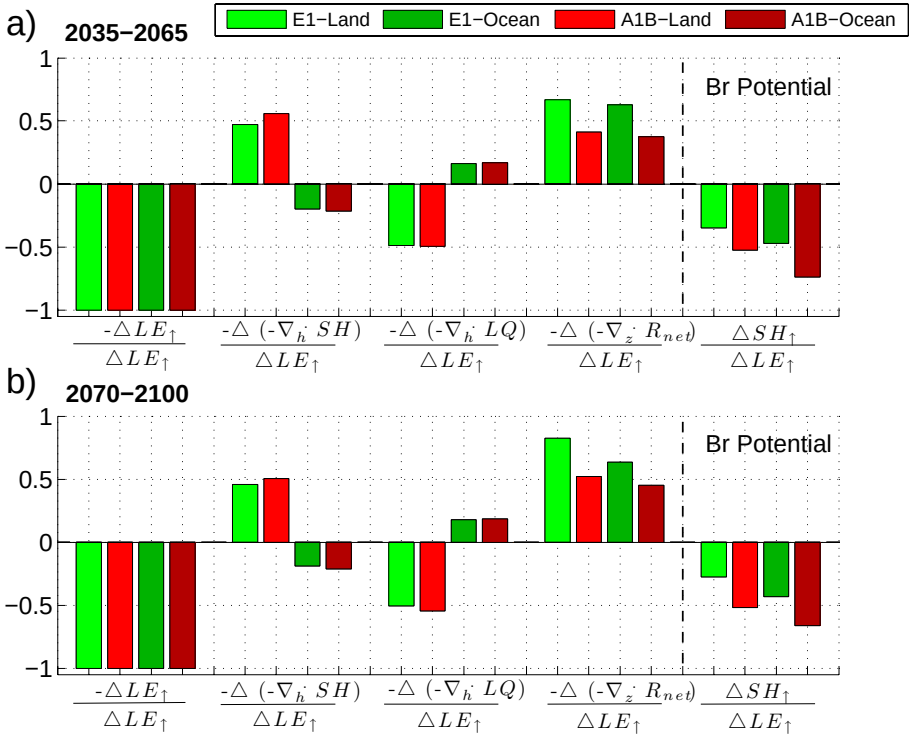

Fig. 12. Land averaged (light colors) and sea averaged (dark colors) contributions to the ratio between surface sensible and latent flux changes (Potential Bowen Ratio; PBr), compared to reference 1970–2000 climatology, for **(a)** 2035–2065 and **(b)** 2070–2100 averages. Contributions from atmospheric convergence of sensible heat ($-\nabla_h \cdot \mathrm{SH}$) and latent heat ($-\nabla_h \cdot LQ$), radiation absorption ($-\nabla_z \cdot R_{\mathrm{net}}$) and surface latent heat ($\mathrm{LE}_\uparrow$) are reported in red for A1B and in green for E1.

ESDD
3, 523–560, 2012